ELSEVIER

Journal of Fluids and Structures 25 (2009) 245–262

JOURNAL OF FLUIDS AND STRUCTURES

www.elsevier.com/locate/jfs

Vortex shedding flow behind a slowly rotating circular cylinder

K.M. Lam*

Department of Civil Engineering, The University of Hong Kong, Pokfulam Road, Hong Kong

Received 7 March 2007; accepted 4 April 2008
Available online 9 July 2008

Abstract

This paper investigates flow past a rotating circular cylinder at $3600 \leqslant Re \leqslant 5000$ and $\alpha \leqslant 2.5$. The flow parameter α is the circumferential speed at the cylinder surface normalized by the free-stream velocity of the uniform cross-flow. With particle image velocimetry (PIV), vortex shedding from the cylinder is clearly observed at $\alpha < 1.9$. The vortex pattern is very similar to the vortex street behind a stationary circular cylinder; but with increasing cylinder rotation speed, the wake is observed to become increasing narrower and deflected sideways. Properties of large-scale vortices developed from the shear layers and shed into the wake are investigated with the vorticity field derived from the PIV data. The vortex formation length is found to decrease with increasing α. This leads to a slow increase in vortex shedding frequency with α. At $\alpha = 0.65$, vortex shedding is found to synchronize with cylinder rotation, with one vortex being shed every rotation cycle of the cylinder. Vortex dynamics are studied at this value of α with the phase-locked eduction technique. It is found that although the shear layers at two different sides of the cylinder possess unequal vorticity levels, alternating vortices subsequently shed from the cylinder to join the two trains of vortices in the vortex street pattern exhibit very little difference in vortex strength.

Keywords: Rotating cylinder; Vortices; PIV

1. Introduction

Flow past a circular cylinder is perhaps the most popular candidate in theoretical, experimental and numerical studies of wake flows. The flow geometry is simple and two-dimensional but the flow actually involves complex interaction of instabilities, secondary vortices and large-scale vortices in three dimensions. Many issues of flow interaction and wake transition are still unresolved. Numerous investigations have been focused on the development and dynamics of the large-scale vortex street shed from the circular cylinder [e.g., Cantwell and Coles (1983)]. This is because these vortices are largely responsible for physical processes associated with the flow, such as heat transfer, fluid mixing and noise generation.

Vortex shedding can be modified by imposing controllable movements on the cylinder. A matching of cylinder movement with the natural vortex shedding of the cylinder results in the lock-in resonance phenomenon, where vortices are shed in synchronization with cylinder movement. In most studies of this kind, the cylinder is given an oscillating motion, either in-line, laterally, or in rotation. For a cylinder oscillating in the lateral direction, lock-in occurs when the oscillating frequency of cylinder movement synchronizes with the natural vortex shedding frequency which is the

*Fax: +852 2559 5337.
E-mail address: kmlam@hku.hk

0889-9746/$ - see front matter
doi:10.1016/j.jfluidstructs.2008.04.005

frequency of the fluctuating lift (Ongoren and Rockwell, 1988). For in-line oscillations, lock-on occurs when the frequency of cylinder oscillation approaches the frequency of the fluctuating drag force due to natural vortex shedding, which is twice the natural vortex shedding frequency (Griffin and Ramberg, 1976). For a rotationally oscillating cylinder, synchronization between vortex shedding and cylinder movement occurs when the cylinder oscillation frequency is near to the natural vortex shedding frequency (Okajima et al., 1975). During lock-in, vortex shedding and the pattern of vortices possess a high degree of regularity and two-dimensionality. This facilitates experimental study of the shedding mechanism, and of the development and dynamics of the vortex street (Lam, 1996). Oscillating movement of the cylinder at frequencies away from the natural vortex shedding frequency, in particular at a very high speed, can lead to suppression of vortex shedding.

Interaction of flow with cylinder movement also occurs for a circular cylinder which is rotating at a steady speed. From simple consideration of potential flow, cylinder rotation leads to acceleration of flow on one side of the cylinder and flow deceleration on the other side. The associated pressure difference results in a mean lift force, and this is referred to as the Magnus effect. The flow is governed mainly by two flow parameters: the Reynolds number Re and the nondimensional rotation speed α. The parameter α is the ratio of circumferential speed at the cylinder surface to free-stream velocity of the uniform cross-flow, that is $\alpha = \omega D/2U_\infty$. Here, D is the diameter, ω is the angular rotation speed of the cylinder, and U_∞ is the free-stream velocity.

Very few experimental investigations have been reported in the literature on flow past a rotating circular cylinder (Badr et al., 1990; Kimura et al., 1992). Wake pattern and possible vortex shedding were studied by flow visualizations only and most experiments were carried out at cylinder rotational speeds below $\alpha \leqslant 2.5$. Vortex shedding from the cylinder in the form of a vortex street was observed at α below a critical value. The critical rotation speed was found to be about $\alpha < 2.0$ at $\mathrm{Re} > 1000$ (Badr et al., 1990). As α increased from zero, the cylinder wake was observed to deflect to one side and the wake became asymmetric (Kimura et al., 1992). Quantitative measurement of velocity fields and velocity-derived quantities such as vorticity has not been reported, and this seriously limited the understanding of vortex dynamics in the wake of a rotating cylinder.

More information on the wake and vortex shedding from a rotating circular cylinder has been obtained from numerical studies. Kimura and Tsutahara (1987) modelled the wake formation with the discrete vortex method and reproduced their experimental observation of a narrower, more deflected and asymmetric wake pattern at increasing values of α. Ingham (1983) attempted to compute the flow at $\mathrm{Re} = 5$ and 20 and cylinder rotation speeds up to $\alpha = 0.5$. Kang et al. (1999) simulated the flow at higher Re and faster cylinder rotation up to $\mathrm{Re} \leqslant 160$ and $\alpha \leqslant 2.5$, while Chew et al. (1995) used a hybrid vortex scheme to investigate vortex shedding from the cylinder at $\mathrm{Re} = 1000$ and $\alpha \leqslant 6$. These studies confirmed the existence of a critical rotational speed, above which vortex shedding cannot be observed. In Kang et al. (1999), the critical value of α was found to increase with Re. Numerical studies also have the ability to study flows at very high values of α which are difficult to achieve in experiments (Sengupta et al., 2003). Recent numerical studies at high rotational speeds detected the presence of a second mode of vortex shedding at $\alpha > 4.35$ or 4.8 (Mittal and Kumar, 2003; Stojkovic et al., 2003).

The objectives of this paper are to investigate experimentally the vortex shedding flow from a rotating circular cylinder and to obtain velocity field information in the wake using particle image velocimetry (PIV). The experiments are carried out at $3600 \leqslant \mathrm{Re} \leqslant 5000$ and the focus is on the asymmetric wake with vortex shedding. The rotation speeds being studied are $\alpha \leqslant 2.5$. It is hoped that the PIV results can provide velocity and vorticity data for the understanding of flow over a rotating cylinder and for comparison with numerical experiments.

2. Experimental techniques

Experiments were carried out in a wind tunnel with an octagonal test-section of width 44 cm. The free-stream flow was uniform, to within 1%, across the middle 90% of the test-section and the turbulence intensity was below 0.01 (Lam, 1996). A circular cylinder of diameter $D = 3.81$ cm was mounted horizontally in the test-section. It protruded through the wind tunnel wall at either side. The cylinder was made of aluminium and the surface was painted black for better optical effects. A stepper motor was used to drive the cylinder to rotate about its longitudinal axis. The speed of rotation was precisely controlled and set at a constant value ω for a particular set of experiments. Experiments were performed at a number of rotation speeds between $0 \leqslant \alpha \leqslant 2.5$. Free-stream velocities at values between $U_\infty = 1.4$ and 2.0 m/s were used in different sets of experiments. The Reynolds number was between $\mathrm{Re} = U_\infty D/\nu = 3600$ and 5000.

PIV was used as the main investigation tool to study the flow in the wake. The PIV system has been described previously (Lam and Leung, 2005). Dispersed smoke carried by flow on the central longitudinal plane at the mid-span of the circular cylinder was illuminated by a laser sheet from a dual Nd:YAG laser with energy 2×150 mJ. A PIV

camera (PCO Sensicam) was used to capture the pair of double-pulsed particle images on two successive image files. The digital flow images covered a region of about $6.2D$ and $3.8D$ in the streamwise and lateral directions in resolutions 1024 pixels × 640 pixels. With interrogation windows of size 32 pixels × 32 pixels and 50% overlap among windows, PIV vectors were obtained on a regular grid of 71 points × 39 points. The PIV algorithm, which was based on the double-pulse cross-correlation technique (Willert and Gharib, 1991), included sub-pixel analysis with three-point Gaussian fitting and the uncertainty in velocity measurement was estimated to be 0.015 m/s, that is about $0.01U_\infty$. Streamlines and vorticity distribution were computed from the velocity field. Vorticity at a grid point was calculated from the circulation around the eight neighbouring grid points. The uncertainty in the vorticity calculation is estimated at about 2%.

Qualitative observations on vortex patterns in the wake were made with smoke visualizations. Dense smoke was released from a smoke wire placed at a distance of a few cylinder diameters upstream of the cylinder. The laser sheet provided an enhanced two-dimensional view of the flow. A shaft encoder was installed on the stepper motor so that, if needed, PIV or smoke visualizations could always be made at a fixed rotation phase of the cylinder. For each value of α, 100 PIV snapshots and 100 smoke visualization images were taken. It would be desirable to have a larger ensemble size of PIV realizations but the calculation of velocities in the present PIV system was performed with Matlab on digitally stored particle images so that the computation resources were very demanding. Results of statistical analysis of the velocity-derived vorticity data, which will be presented later, suggested that the chosen ensemble size could provide some meaningful statistics of flow phenomena.

Hot-wire measurements were made to detect vortex shedding and to determine the vortex shedding frequency. A pair of hot wires were placed at a downstream distance of $x/D = 5$ and on two sides on the wake at $y/D = \pm 1.0$ to measure velocity fluctuations due to passage of vortices. The origin of the coordinate system was at the centre of the cylinder. As shown in later figures, the free-stream flow is from left to right with the streamwise x-coordinate increasing. The cylinder rotates in the clockwise direction and the y-coordinate is positive upwards.

3. Results and discussion

3.1. Vortex shedding frequency

Previous investigations have established that vortex shedding in the form of a vortex street occurs at low nondimensional rotation speeds, $\alpha \leqslant 1.2$ (Badr et al., 1990; Kang et al., 1999). The numerical results of Kang et al. (1999) at Re up to 160 showed that the vortex shedding frequency or St is nearly independent of α but increases with Re. The values of St in their investigation varied from 0.135 to 0.19 as Re increased from 60 to 160. However, the numerical study of Chew et al. (1995) at a much higher Re, Re = 1000, found that St increases slowly with α: from St = 0.21 to 0.24 as α increased from 0 to 2. They further argued that the increase of St was associated with the observed narrowing of the wake as α increases. In the present experiments, velocity fluctuations on opposite sides of the wake have been measured with two hot wires. The cross-correlation functions between the two velocity signals are computed at different values of α to detect vortex shedding. For $\alpha \leqslant 1.2$, curves of time-lagged cross-correlation coefficient $R(\tau)$, not shown for brevity, exhibits near-sinusoidal shape. Peak negative coefficient at $R \approx 0.4$ is found near zero time-lag. This is typical of the existence of a street of alternating vortices. As α increases further, the curve of $R(\tau)$ departs from the sinusoidal shape and the peak coefficient drops in value. This suggests that the alternating vortices become less periodic or less coherently spaced. At $\alpha \geqslant 1.92$, the two hot-wire signals are almost totally uncorrelated with curves of $R(\tau)$ not showing any periodicity. These results are consistent with Badr et al. (1990) that vortex shedding stops when the cylinder rotation speed exceeds $\alpha \approx 2$.

Another observation in the cross-correlation curves is that the period of the $R(\tau)$ curves decreases as α increases. The vortex shedding frequency, f_s, is calculated from this time period as well as from power spectra of the hot-wire signals. Fig. 1 shows the variation of Strouhal number, $\mathrm{St} = f_s D/U_\infty$, of vortex shedding with α. It is observed that St increases slowly from 0.18 to 0.29 as α increases from 0 to 1.68. Numerical results from Chew et al. (1995) at Re = 1000, included in Fig. 1, show a much slower rate of increase of St with α. A decrease of St with α is found in the computation of Kang et al. (1999) at the much lower Re = 160.

Fig. 1 also shows the cylinder rotation frequency as $\omega D/2\pi U_\infty$. Around $\alpha = 0.65$, the vortex shedding frequency appears to be the same as the cylinder rotation frequency. In other words, a vortex is shed from the same side of the cylinder every complete rotation of the cylinder. This provides a convenient way for studying the vortex pattern by phase-locking PIV measurement or flow visualization at a fixed cylinder rotation phase which synchronizes with vortex shedding at this value of α. The coincidence relationship between vortex shedding and cylinder rotation is studied with cross-correlation measurements of the hot-wire signal in the wake with the sinusoidal signal of cylinder rotation angle.

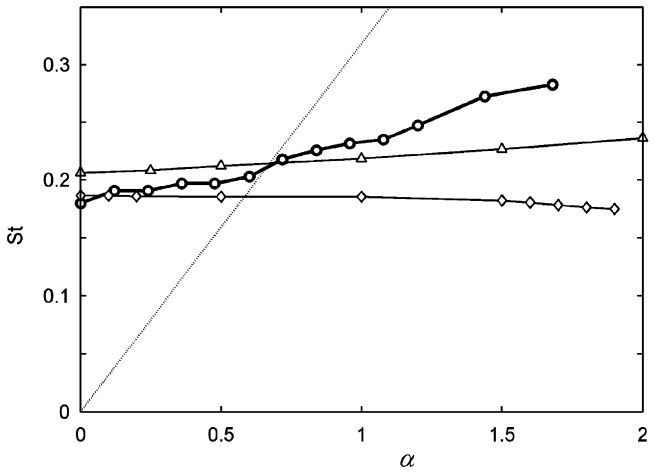

Fig. 1. Variation of Strouhal number of vortex shedding with cylinder rotation speed. Broken line shows frequency of cylinder rotation. Present data: (○) Re = 5000; Chew et al. (1995): (△) Re = 1000; Kang et al. (1999): (◇) Re = 160.

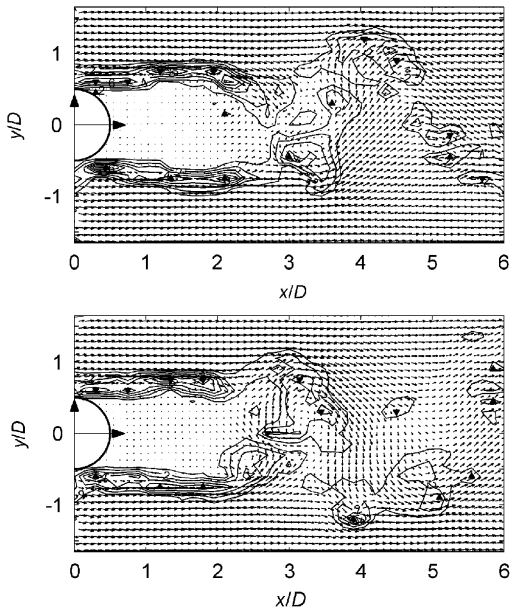

Fig. 2. PIV snapshots for the stationary cylinder ($\alpha = 0$): vorticity contours at $\zeta' = \zeta D/U_\infty = \{\pm 1, \pm 2, \pm 3, \ldots\}$. Vorticity crests and valleys marked.

The results, not shown here, show a very high level of correlation near $\alpha = 0.65$, confirming the synchronization between vortex shedding and cylinder rotation.

3.2. Instantaneous wake patterns

Flow in the wake behind the cylinder is highly turbulent. Vortices shed from the cylinder exhibit feature variations such as strengths, shapes and paths. For the stationary cylinder ($\alpha = 0$), Fig. 2 shows examples of two instantaneous PIV snapshots. A street of alternating vortices is revealed by these instantaneous velocity fields and vorticity contours. From manual examination, almost all the ensemble of 100 PIV snapshots show the presence of at least one shed vortex in the wake with closed contours of vorticity concentration.

Vorticity contours, such as those in Fig. 2, are useful in revealing the location and strength of vortices and shear layers shed from the cylinder. As the first simple analysis, locations and levels of vorticity crests and valleys are extracted from the PIV snapshots. These peaks are local maxima and minima in the vorticity distribution. Fig. 3(a) shows locations of all vorticity peaks found in the ensemble of 100 PIV snapshots for the stationary cylinder. Vorticity peaks are found along the two separation shear layers from the cylinder. Vorticity is fed into a large-scale vortex which stays centred near $x/D \approx 2.5$ for some time to build up its fluid circulation. Levels of the vorticity peaks, in nondimensional form of $\zeta' = \zeta D/U_\infty$, are plotted against x/D in Fig. 4(a). Upstream of $x/D \approx 2.5$, the vorticity peaks are located inside the shear layers and the peak levels stay at a constant high level. Vorticity is fed from the shear layer into the attaching vortex located around $x/D \approx 2.5$. The vortex grows and accumulates fluid circulation. Large variations in peak vorticity levels around $x/D \approx 2.5$ are evident in Fig. 4(a). This is believed to be due to attaching vortices at different stages of growth. After accumulating sufficient fluid circulation, the attaching vortex is shed downstream into the wake. While being convected downstream in the wake, the shed vortex is cut off from further supply of fluid circulation from the shear layer. Diffusion of the peak vorticity level at its centre occurs, and Fig. 4(a) shows a drop in peak vorticity levels from a mean value of $\zeta' \approx 5.5$ at $x/D = 2.5$ to $\zeta' \approx 4.5$ at $x/D = 6$. Alternating vortices of opposite signs of rotation are observed to possess equal strengths or vorticity levels at the same streamwise locations.

It is clearly observed from Fig. 3(a) that a "vortex formation length" at $2.5D$ is required for the formation of the large-scale vortices to be shed in the form of a vortex street. The vortex formation length behind a circular cylinder has been found to depend on Re and the present value of $2.5D$ is consistent with published data at Re in the order of 10^3 (Green and Gerrard, 1993; Ozono, 1999). Fig. 3(a) shows that there exists much scatter in the locations of vorticity crests and valleys for the vortices in the wake. This is partly caused by jitter in locations and paths of the vortices because natural vortex shedding is not a totally regular and repeatable process. Another reason is that the vorticity crests and valleys from PIV data do not always show the exact centre location of the large-scale vortices as shown by the vorticity contours in Fig. 2.

PIV measurements and flow visualizations have been made behind the cylinder rotating at different values of α. Fig. 5 shows examples of two PIV snapshots at $\alpha = 0.6$. The cylinder is rotating in the clockwise direction. The two PIV snapshots chosen show roughly opposite phases of the vortex-shedding cycle. At this low rotation speed of the cylinder, the vortices are shed along paths which are only slightly deflected from the free-stream direction. However, it is evident that the vortices are shed at a much shorter distance from the cylinder when compared to Fig. 2. The vortex formation

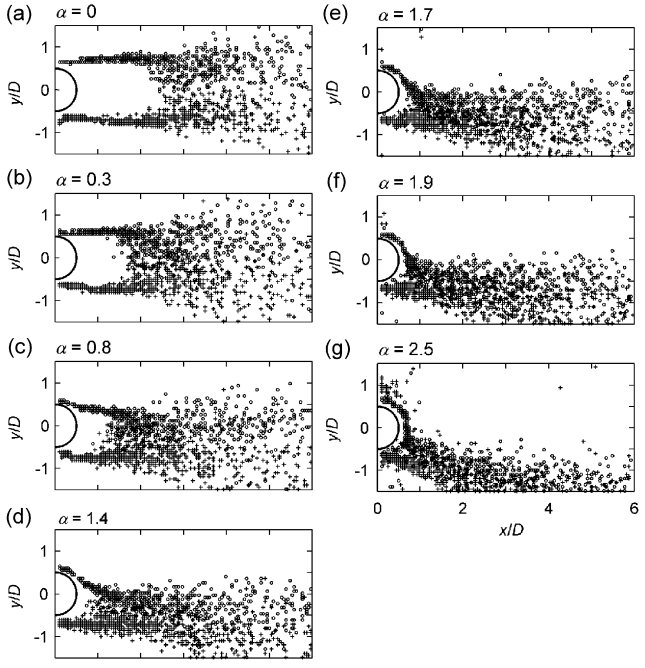

Fig. 3. Locations of vorticity crests and valleys in the ensemble of 100 PIV snapshots: (+) positive vorticity; (○) negative vorticity.

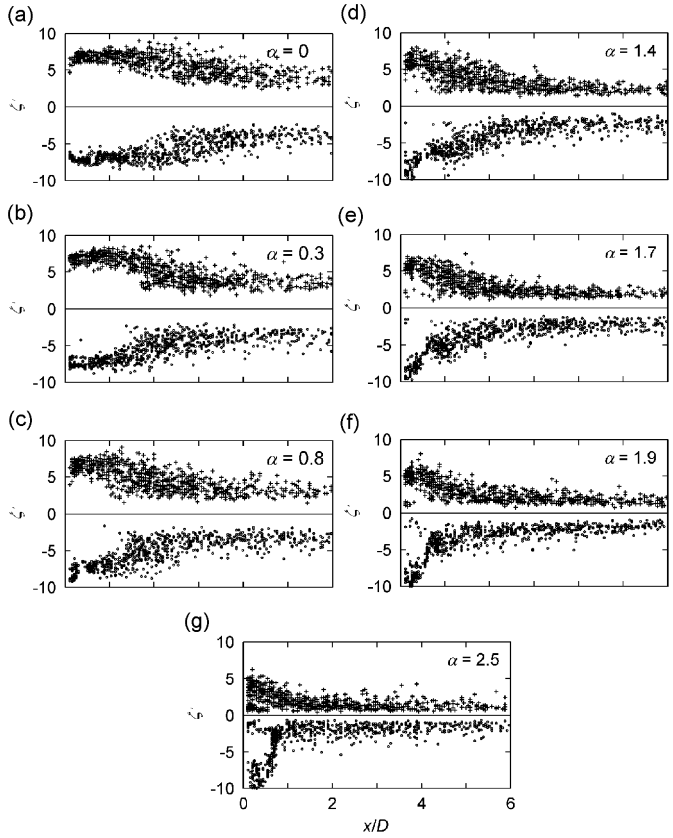

Fig. 4. Variation of peak vorticity levels with downstream locations for vorticity crests and valleys in Fig. 3: (+) positive vorticity in lower side of wake; (●) negative vorticity in upper side of wake.

length becomes shorter from $2.5D$ for $\alpha = 0$ to about $1.65D$ in Fig. 5. This shortening of vortex formation length with α is more evidently shown by the locations of vorticity peaks in Fig. 3.

PIV snapshots for the cylinder rotating at some other values of α are shown in Figs. 6–9. The values are $\alpha = 1.1$, 1.7, 1.9 and 2.5, respectively. Results at other values of α are not shown for brevity but the data of vorticity peaks have been included in Figs. 3 and 4. Analysis of vortex properties is carried out on PIV snapshots at all values of α and the results are shown in Fig. 12. Comparing the results at different cylinder rotation speeds, a number of observations can be made on the effect of α on the wake pattern and vortex shedding. The wake pattern behind the cylinder at $\alpha = 0.3$ remains largely similar to that at $\alpha = 0$. The vortices are shed along paths parallel to the free-stream direction and the wake width is similar to that of the stationary cylinder. However, it is evident that the vortex formation length becomes shorter, from $2.5D$ to about $1.8D$ (Fig. 3). At $\alpha = 0.6$, some deflection of the vortex paths is observed in Fig. 5 and the vortex formation length decreases to $1.65D$. The trend continues to $\alpha = 0.8$ at which the wake is clearly observed to be deflected to one side (Fig. 3(c)). The deflection is towards the lower side of the rotating cylinder which is moving against the free-stream. When the cylinder rotation speed increases to $\alpha = 1.1$, Fig. 6 shows that the shear layer on the upper side of the cylinder is brought downward due to the high-speed rotation of the cylinder. The lower shear layer can still roll up to form vortices. With time, the attaching vortex from either shear layer protrudes into the opposite shear layer to detach the other vortex into the wake. Although the vortex formation length is greatly shortened to about $1.2D$, alternating vortex shedding is still observed in over 90% of the ensemble of smoke images. This approximate percentage is obtained by manual observation and counting of the 100 smoke images in the ensemble, as well as the 100 PIV snapshots. Actually, a very high percentage of observation at about 90% of shedding of alternating vortices is made from $\alpha = 0$ to this value of α. The percentage then starts to drop to about 75% at $\alpha = 1.4$ and 1.6. At $\alpha = 1.8$, only about 50% of the smoke images show clear patterns of alternating vortices in the cylinder wake. This further drops to 25% at $\alpha = 2.0$.

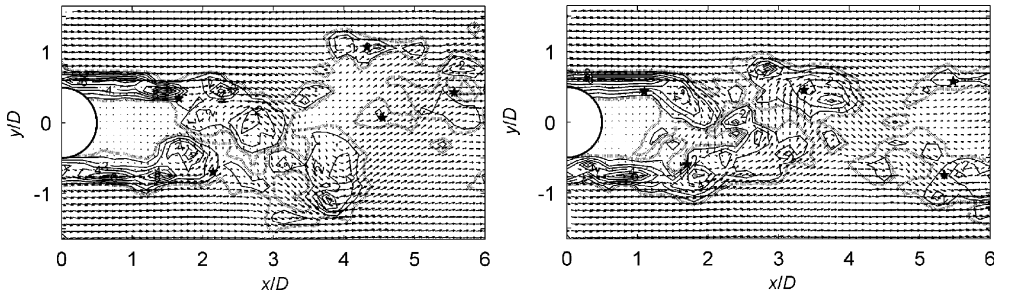

Fig. 5. PIV snapshots for cylinder rotating at $\alpha = 0.6$: vorticity contours at $\zeta' = \{\pm 1, \pm 2, \pm 3, \ldots\}$. Identification of vortex regions: closed contours of threshold vorticity level at $\zeta' = \pm 0.5$ marked by thick lines; centre positions marked by asterisk (*).

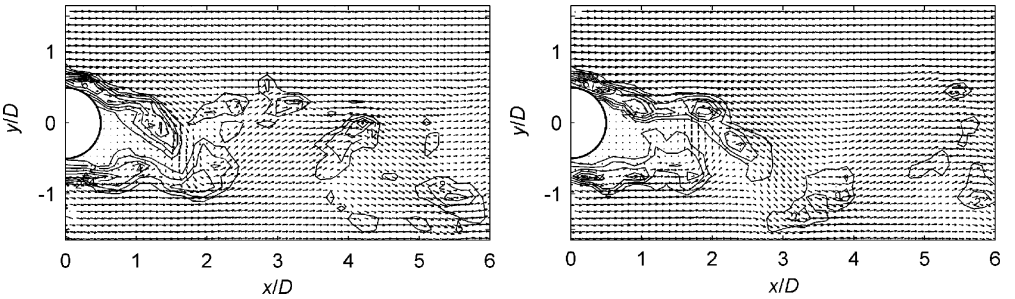

Fig. 6. PIV snapshots for cylinder rotating at $\alpha = 1.1$: vorticity contours at $\zeta' = \{\pm 1, \pm 2, \pm 3, \ldots\}$.

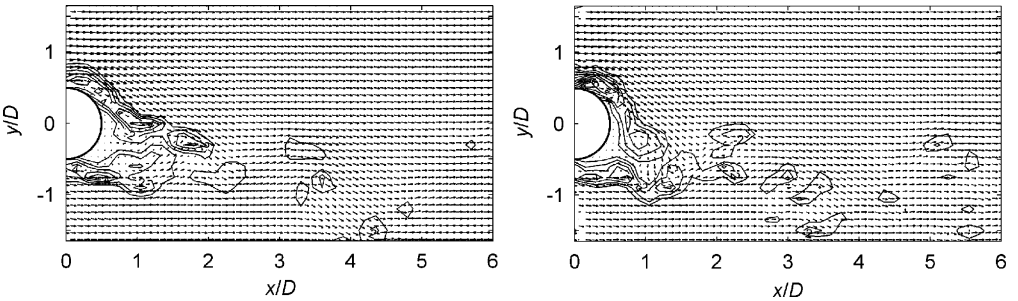

Fig. 7. PIV snapshots for cylinder rotating at $\alpha = 1.7$: vorticity contours at $\zeta' = \{\pm 1, \pm 2, \pm 3, \ldots\}$.

Fig. 7 shows the instantaneous wake patterns at $\alpha = 1.7$. With more deflection of the wake to one side, the wake width is shortened further. This is accompanied by smaller sizes of the vortices and very short vortex formation length at about $0.8D$ (Fig. 3). At $\alpha = 1.9$, evidence of shedding of alternating vortices is observed from the selected snapshots in Fig. 8 but patterns as those shown are observed in only 25% of the PIV snapshots or smoke images. Fig. 3 shows that the vortex formation length, if still meaningful at this high cylinder rotation speed, is only slightly longer than the shortest possible value of $0.5D$. Examples of PIV snapshots at $\alpha = 2.5$ are shown in Fig. 9. In most of the PIV snapshots, there is a region of vorticity concentration circumscribing the upper half of the leeward face of the cylinder. On the lower side is another smaller region of vorticity concentration. Unlike the cases of lower cylinder rotation speeds, these two vorticity regions exhibit little lateral waggling among the snapshots in the ensemble. There is also no evidence of a growing vortex into which the shear layers feed vorticity. In only a few PIV snapshots out of the 100 samples exist enclosed regions of vorticity concentration downstream of the shear layer. One of those snapshots is shown as the second example in Fig. 9. The smoke images at this value of α, not shown here, do not show evidence of well-defined vortices behind the cylinder.

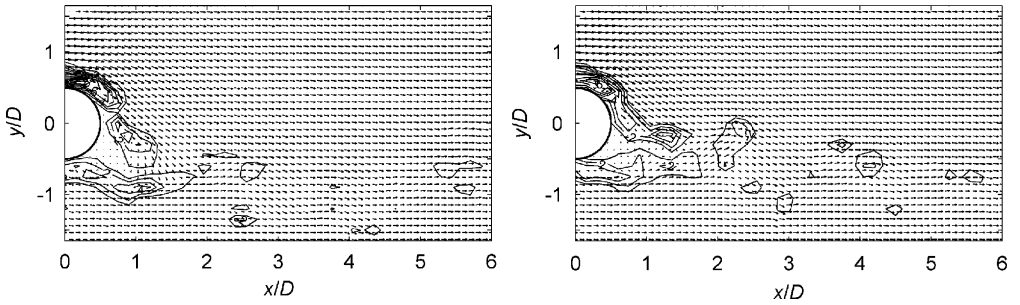

Fig. 8. PIV snapshots for cylinder rotating at $\alpha = 1.9$: vorticity contours at $\zeta' = \{\pm 1, \pm 2, \pm 3, \ldots\}$.

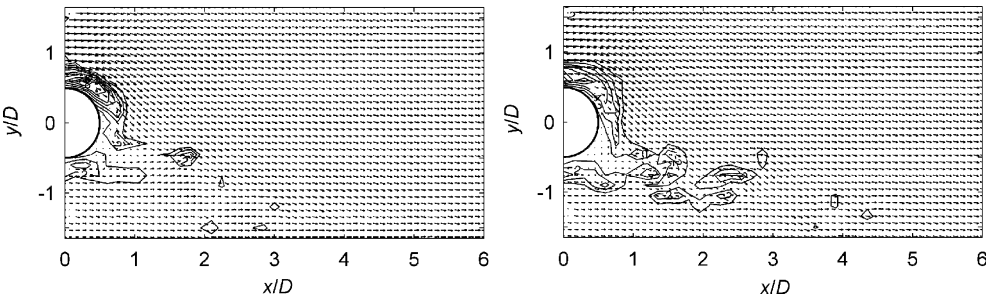

Fig. 9. PIV snapshots for cylinder rotating at $\alpha = 2.5$: vorticity contours at $\zeta' = \{\pm 1, \pm 2, \pm 3, \ldots\}$.

3.3. Vortex properties

The locations and levels of vorticity peaks shown in Figs. 3 and 4 provide simple statistics and indication of the vortex paths and strengths. Fig. 4 shows that as α increases, the strength of the vortices in the wake, as measured by the peak value of ζ', becomes lower at same streamwise locations. The rate of drop of peak vorticity level with downstream distance x also becomes much faster at higher values of α. In the asymmetric wake flow behind an inclined flat plate, unequal vortex strengths at same streamwise locations are found for the two trains of alternating vortices (Lam and Leung, 2005). This unequal vortex strength is not so evidently observed in Fig. 4 for flow over a rotating cylinder which also exhibits an asymmetric wake pattern. Beyond the vortex formation length, no noticeable difference in peak vorticity levels can be observed in Fig. 4 for the two trains of shed vortices of opposite signs of rotation. At $\alpha \geqslant 0.8$, a discontinuity of ζ' with x is observed at $x/D \approx 0.5$ on the upper trains of vortices. In the upper shear layer, flow near the cylinder surface occurs at high velocities because the cylinder surface moves with a downstream velocity component due to rotation. This velocity could not be measured with the present PIV system due to the always-stationary image of the rotating cylinder. The neglect of cylinder surface velocity results in an erroneously magnified value of ζ in the upper shear layer close to the cylinder surface. Hence, the data of ζ' before the discontinuity of $\zeta'(x)$ in Fig. 4(c), (d) and (e) should be discarded.

In addition to simply using local maxima and minima in the vorticity distribution to identify vortices, another more elaborate method of vortex identification is attempted. The procedures are illustrated with the aid of PIV snapshots in Fig. 5. The region of vorticity concentration around each vorticity peak and enclosed by the contour line $\zeta' = -0.5$ or $\zeta' = 0.5$ is identified as an individual vortex region or "vortex". After a vortex region is identified by this chosen threshold of $\zeta' = \pm 0.5$, its properties are computed. The vortex properties include the "vortex size" which is the area Λ of enclosed vortex region, the total amount of fluid circulation Γ inside this region, and the centre position of the "vortex". The centre position is calculated from the vorticity-weighted centroid of the vortex region. The "vortex" regions identified in the two PIV snapshots in Fig. 5 and their centre positions are marked in the figure. It is noted that this automatic analysis cannot distinguish the shear layers from the large-scale vortices. Regions of unreasonably small enclosed areas are discarded in the vortex identification process. The threshold vorticity magnitude used to identify the vortex regions has been somewhat arbitrarily chosen at $\zeta' = \pm 0.5$. The effect of this threshold has been investigated by using two other values of threshold, at $\zeta' = \pm 0.25$ and $\zeta' = \pm 1$. The detailed comparison is not presented here for

brevity. It is found that using the smaller threshold value results in fewer vortex regions identified because several regions of vorticity concentration may be enclosed together as one region. This results in bigger sizes and larger fluid circulation amounts for the identified vortex regions. Choosing $\zeta' = \pm 0.25$ or $\zeta' = \pm 0.5$ as the threshold level only leads to slight differences in the statistics of resulting vortex properties, but using $\zeta' = \pm 1$ results in much smaller vortex sizes. It appears that $\zeta' = \pm 0.5$ is an appropriate threshold value. From the size and fluid circulation of a vortex region, the average vorticity level for that vortex can be obtained by dividing the total circulation by the vortex size. This property of Γ/Λ, which gives a measure of the average vorticity level in the vortex region, is found to be less sensitive to the threshold vorticity value chosen for vortex identification.

Fig. 10 shows the vortex properties at different cylinder rotation speeds. The properties of vortex regions which have been identified from the ensemble of all 100 PIV snapshots at $\alpha = 0.6$ are presented in Fig. 10(b). This case is used here for detailed discussion. For either clockwise or counter-clockwise rotating vortices, two groups of vortices are evident from the ensemble of vortex regions identified. More upstream, a vortex region in the first group consists of a shear layer and the attaching vortex into which it feeds vorticity. The vortex can be growing or about to be shed into the wake (Fig. 5). In Fig. 10(b), the lateral coordinates of the centre positions of these "vortices" show little variations among the PIV snapshots. The data of Λ/D^2, however, shows that the "sizes" of the vortices increase roughly linearly with the streamwise locations of their centres. This is because a vortex region always includes the shear layer which starts from the cylinder surface (Fig. 5). When the growing vortex is about to be shed, it is at a more downstream location and the enclosed region of vorticity concentration associated with this vortex covers a larger area. Likewise, a larger total amount of fluid circulation is found for this vortex from the integration of vorticity over the region. The circulation amount Γ of the first group of "vortices" also increases (in magnitude) with the streamwise location of the vortices. The distribution pattern of Γ with downstream distance has a similar shape as that of Λ/D^2 and is not shown for brevity. The average vorticity level of the vortices, in the dimensionless form, $\overline{\zeta}' = (\Gamma/\Lambda)D/U_\infty$, exhibits a more reasonable slowly decreasing trend with the streamwise location. Downstream of the first group, the second group of vortices identified are the vortices already shed into the wake. They are being convected downstream and already cut off from the supply of vorticity from the shear layers. Fig. 10(b) shows that their centre positions and sizes exhibit large ensemble variations. The circulation amounts are much lower in magnitude than those of the growing vortices attached to the shear layer but the average vorticity level remains at consistent levels with little variations in the ensemble.

The effect of cylinder rotation speed α on the vortex properties can be observed in Fig. 10. The centre positions of the first group of vortices are the vorticity-weighted centroids of individual growing vortices which remain attached to the shear layers. It is evident that, as α increases, the vortex centres are more offset to the lower side of the wake and located more upstream to the cylinder. The distance between the two trains of vortices also decreases as α increases. At $\alpha = 1.9$, two trains of vortex centres are still well identified, but at $\alpha = 2.5$ the lower train of vortices, of positive vorticity, cannot be evidently found. At this fastest cylinder rotation speed, regions of negative vorticity are still found on the upper side (Fig. 9) but they only represent the shear layers without the formation of well-developed vortices.

For each value of α, the mean positions of vortex centres of the two groups of vortices are computed from the results in Fig. 10. Fig. 11 shows the effect of cylinder rotation speed on these mean vortex centre positions. The mean streamwise location of the growing vortices provides an estimate of the "vortex formation length". Fig. 11(a) shows that the two trains of vortices give very similar values of this length, and the length decreases with α. The "vortex formation lengths" have also been found from the first occurrence locations of vorticity peaks in Fig. 3. That data are included in Fig. 11(a) and they agree well with the present data. Also shown in the figure are the mean centre positions of the second group of vortices. This position roughly indicates the average or most probable location of the previously shed vortex when a growing vortex is at the vortex formation length. At $\alpha \leqslant 1.9$ where vortex shedding occurs, the mean streamwise distance, or wavelength, between these two vortices remains fairly constant at about $3D$, regardless the cylinder rotation speed or which vortex trains. As the vortex shedding frequency is found to increase with α in Fig. 1, this means that the convection speed of the vortices in the wake also increases with α. This is consistent with the finding in the next section of lesser degrees of velocity defect in the wake of a rotating cylinder. The mean lateral locations of the vortices at different values of α are shown in Fig. 11(b). The sideways deflection of the vortex paths is clearly observed. It is also noted that the train of vortices on the upper side of the wake are deflected more than the lower train. The exception for the growing vortices on the upper side of the wake at $\alpha = 1.7$ and 1.9 is probably due to the lower percentage of vortex formation and shedding at these higher rotation speeds. When the shear layer does not terminate in the formation of a vortex, the vorticity-weighted centroid will mark the centre of the shear layer itself (Fig. 8).

In Fig. 10, the "vortex sizes" of the first group of vortices vary among the PIV snapshots in a systemic manner by the different development stages of the growing vortices. The "sizes" of the shed vortices, on the other hand, are more scattered. Fig. 11(c) shows that the ensemble-mean vortex sizes of the two trains of vortices on either side of the wake are almost equal for all values of α. This is observed for the growing vortices as well as the shed vortices. For the growing vortices, the mean vortex size reduces tremendously with α, from $|\Lambda| \approx 2.9D^2$ for the stationary cylinder to

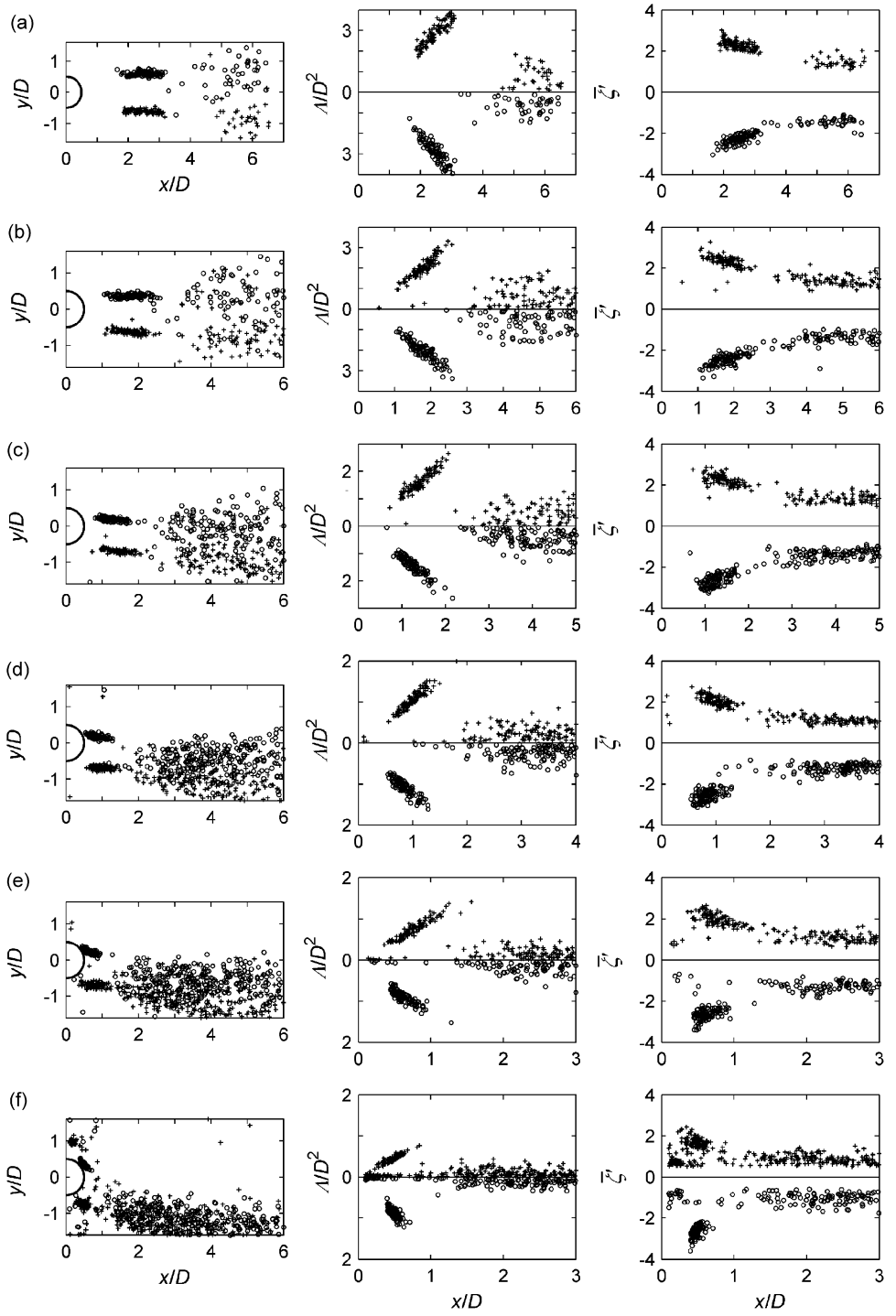

Fig. 10. Vortex properties from ensemble of PIV snapshots at different values of α. Left to right: centre positions, vortex sizes and average vorticity levels: (+) vortices of positive vorticity in lower side of wake; (○) vortices of negative vorticity in upper side of wake.

$|\Lambda| \approx 1.1D^2$ at $\alpha = 1.7$. It should be noted that these sizes include the shear layers (Fig. 5). The mean vortex sizes of the shed vortices vary between $|\Lambda|/D^2 \approx 0.7$ at $\alpha = 0.3$ and $|\Lambda|/D^2 \approx 0.2$ at $\alpha = 1.9$. It can be argued that the vortex sizes have always been obtained from the contour lines at $\zeta' = \pm 0.5$ (Fig. 5) and that different sizes will be obtained from other

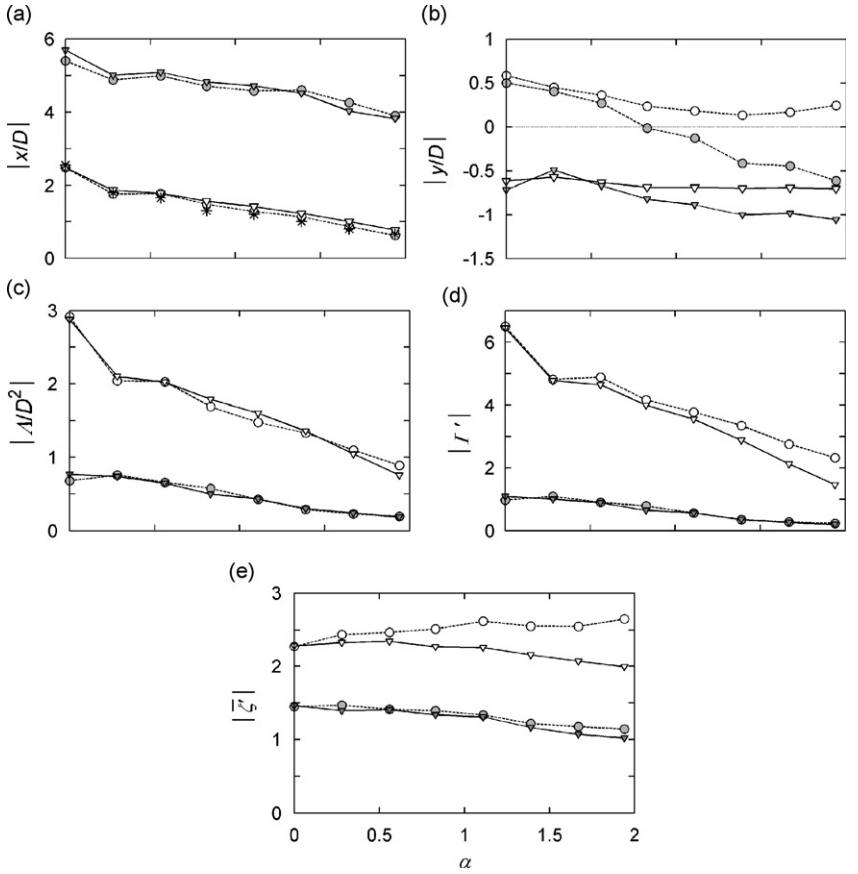

Fig. 11. Variation of mean vortex properties with α: (a, b) centre position: (∗) vortex formation length from Fig. 3; (c) vortex size; (d) circulation; (e) average vorticity level: (▽) vortices of positive vorticity in lower side of wake; (○) vortices of negative vorticity in upper side of wake. Open symbols: growing vortices; filled symbols: shed vortices.

chosen values of ζ'. However, it is also apparent from smoke visualizations, not shown for brevity, that the vortex sizes do decrease with α although not likely as much as three-folds.

The amounts of circulation associated with the vortices, in the nondimensional form Γ'/DU_∞, are shown in Fig. 11(d) to drop very significantly in magnitude with α. Like the vortex sizes, these values are sensitive to the chosen threshold value of ζ'. Fig. 11(e) shows the average vorticity levels over the vortex size for individual vortices. These levels, which are obtained by the quotient of Γ/Λ, should be less sensitive to the threshold vorticity value for vortex identification. The change of these average vorticity levels with cylinder rotation rate is much less significant than the circulation or the vortex size. For the shed vortices in the wake, the levels decrease slightly with α, from $|\overline{\zeta'}| \approx 1.45$ at $\alpha = 0.3$ to $|\overline{\zeta'}| \approx 1.05$ at $\alpha = 1.9$. Very small differences in the magnitude of average vorticity levels are found between the two trains of shed vortices. The growing vortex on the lower side of the cylinder has its average vorticity level, positive in sign, decreasing slightly with α. However, the magnitude of the average negative vorticity level in the growing vortex on the upper side of the cylinder is found to be higher when α increases. This suggests that a higher vorticity production is associated with the upper shear layer as the cylinder rotates at a higher speed.

3.4. Time-averaged wake

The time-averaged mean flow field at each value of α is obtained by averaging all 100 PIV snapshots. Fig. 12 shows, for some selected values of α, the mean velocity vectors and the streamline patterns computed from them. They show clearly the sideways deflection and narrowing of the wake as α increases. The change is gradual for $\alpha < 1$ but becomes more drastic when α increases beyond unity. The region with reverse or very small velocities behind the cylinder is shown to be shortened with increasing α. Shedding of wake vortices takes place near the end of this region which

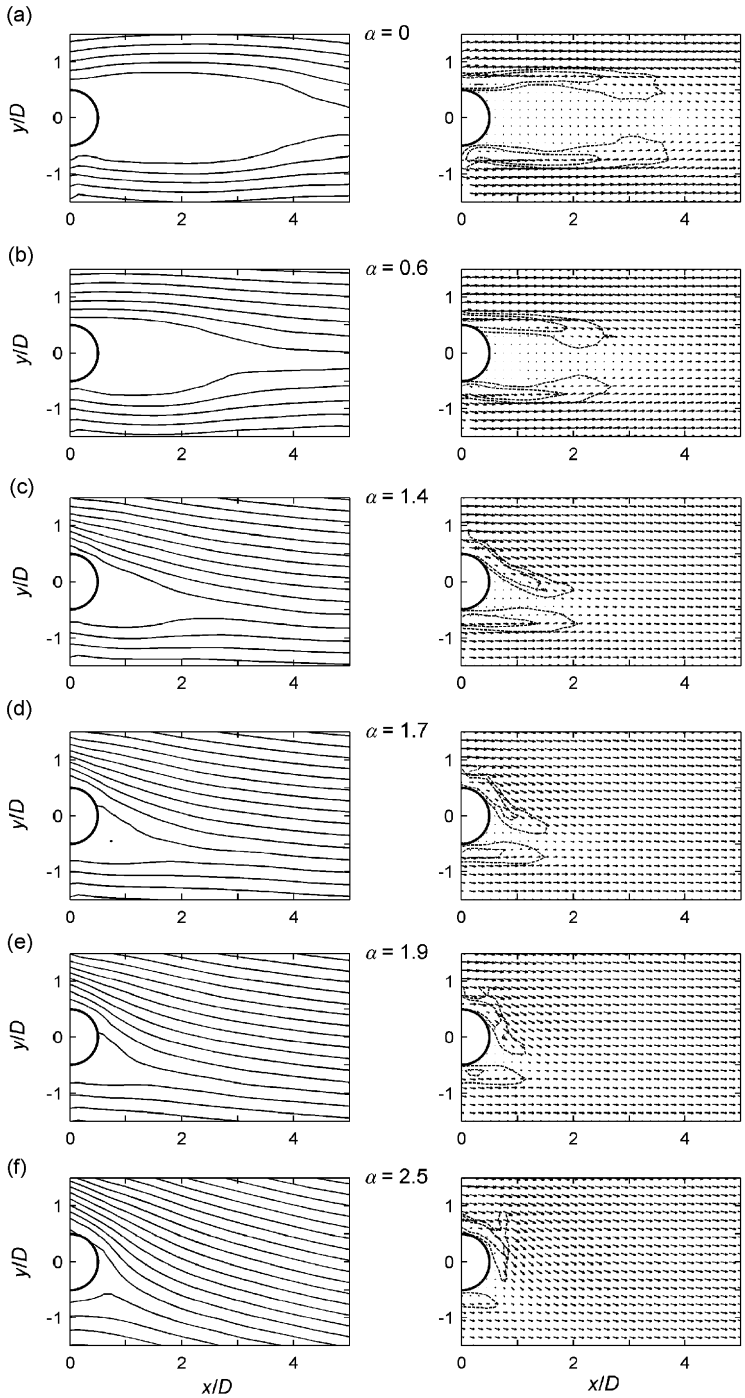

Fig. 12. Averaged flow fields. Left panels: streamlines; right panels: mean velocity vectors with vorticity contours outlined at $\zeta' = \{\pm 1.5, \pm 3, \pm 6\}$.

roughly marks the vortex formation length. A few contours of mean vorticity are included in Fig. 12. Because the PIV snapshots are taken at instants not related to any particular vortex-shedding phase, flow circulation and vorticity contours associated with individual vortices such as those shown in Figs. 5–9 are smoothed out in the average flow field. The vorticity contours follow roughly along the streamlines from the two sides of the cylinder. They mark the mean

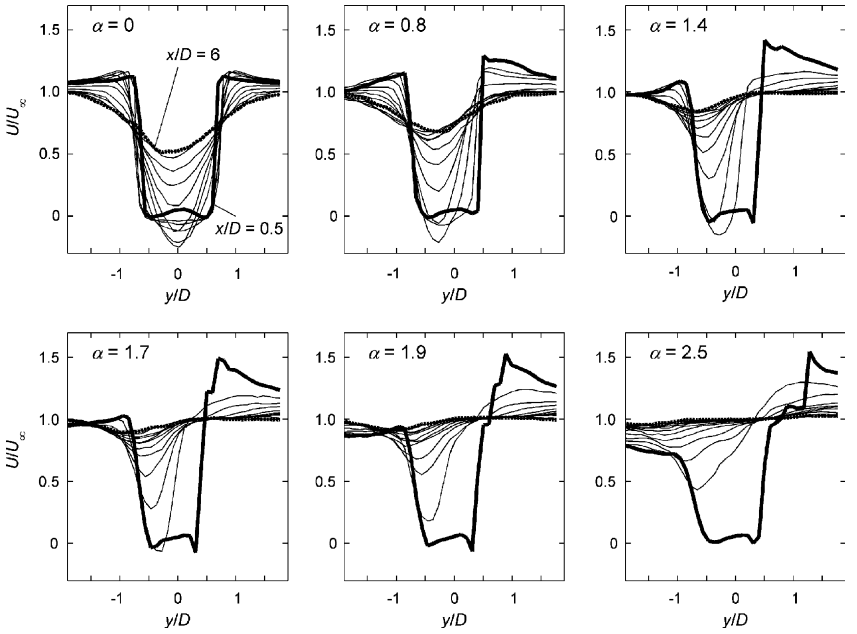

Fig. 13. Lateral profiles of mean streamwise velocity. Downstream stations at $x/D = \{0.5, 1, 1.5, 2, \ldots, 5, 5, 6\}$: first and last stations at $x/D = 0.5$ and 6 in bold lines.

location of the shear layers. At $\alpha \leqslant 1.4$, the wider downstream ends of the lowest-level contour lines show the approximate locations of the large-scale vortices just prior to shedding.

A clearer picture of the velocity defect in the wake can be obtained in Fig. 13 which shows profiles of mean streamwise velocity $U(y)$ at successive downstream stations of x/D. Rotation of the cylinder increases the velocities of flow passing the upper side of the cylinder and reduces the flow velocities near the lower side. Theoretical values of flow velocities under maximum increase or decrease are $U = \pm\alpha U_\infty$ and occur just next to the cylinder surface at $x/D = 0$ and $y/D = \pm 0.5$. Laterally away from the cylinder surface, flow velocities revert to $U = U_\infty$. The present PIV system does not have sufficiently fine resolution to capture flow velocities just outside the cylinder. In addition, the stationary image of the cylinder in the dual PIV images precludes accurate determination of flow velocities near the cylinder. Hence, the first streamwise station with reliable data of $U(y)$ is at $x/D = 0.5$. For the stationary cylinder, the velocity profile there shows velocities faster than the free-stream when fluid accelerates past the two sides of the cylinder. A velocity defect with maximum value of about 0.4 the free-stream velocity is still found at the last station of $x/D = 6$. At $\alpha = 0.8$, the increase in $U(y)$ induced by cylinder rotation in the upper side of the wake (positive y values) is observed at $x/D = 0.5$. No decrease in $U(y)$ is, however, observed in the lower side of the wake. Instead, some flow acceleration is found. This suggests that the backward cylinder velocity has little decelerating effect on flow past the lower cylinder side, as compared to the accelerating effect on the upper cylinder side. Hence, a smaller velocity shear, $\partial U/\partial y$, occurs in the lower shear layer than the upper shear layer. This partly explains the lower values of $|\tilde{\zeta}'|$ observed in Fig. 11(e) for the growing vortex attached to the lower shear layer. The velocity defect in the wake of the rotating cylinder is found to recover at a much faster rate than the stationary cylinder. The smaller wake size is more evident at $\alpha \geqslant 1.4$. When α increases to 1.7, the initial velocity defect region at $x/D = 0.5$ becomes much narrower and this is mainly due to the lateral deflection of the upper shear layer. At $\alpha = 1.9$, velocities lower than the free-stream values begin to appear on the lower side of the cylinder. On the other hand, the upper shear layer is under very high velocity shear due to the increase in velocities with the forward rotation of the cylinder there. This may explain the high vorticity level there in Fig. 12.

Similar mean patterns of the wake are observed in the averaged smoke images which are not shown here for brevity. There is a smoke-free region behind the cylinder which roughly coincides with the region of low flow velocities in Fig. 12.

3.5. Vortex dynamics

Fig. 1 shows that at $\alpha \approx 0.65$, there is synchronization of vortex shedding with cylinder rotation. This synchronization is of a coincident nature and does not involve physical connection between the two processes. Nevertheless, this provides a convenient way for eduction of vortex dynamics at a fixed phase of vortex shedding. With a shaft encoder,

PIV snapshots have been taken at instants during which the cylinder rotates to a particular angle, say $\theta = \theta_1$, in experiments at $\alpha = 0.65$. Most PIV realizations in this ensemble of 100 snapshots are found to exhibit very similar velocity fields. This is because they are at almost the same phase of vortex shedding in different but regular and repetitive vortex-shedding cycles. To educe the large-scale coherent structures in the wake, all PIV snapshots taken at $\theta = \theta_1$ are averaged. This removes the small-scale random turbulent variations to produce a clear pattern of the coherent structures.

Fig. 14(a) shows the velocity vectors and vorticity field associated with the large-scale coherent vortical structures at phase $\theta = \theta_1$ of the vortex-shedding cycle. A mature rolled-up vortex can be observed on the upper side of the cylinder. It is centred roughly at $x/D = 1.8$ which is just beyond the average vortex formation length at this value of α (Fig. 11(a)). The vortex has just been shed, and very high level of vorticity at $\zeta' = \zeta D/U_\infty \approx -3$ is still found at the vortex centre. Even higher magnitudes of vorticity at $\zeta' < -6$ are found in the upper shear layer. When the vortex was still attached to the cylinder, the upper shear layer has fed vorticity into it for its growth. On the lower side of the wake, a counter-clockwise rotating vortex is found convecting downstream with its centre at $x/D \approx 2.8$. Although the vorticity contours are connected to those of the shear layer from the lower side of the cylinder, the vortex has been shed and is cut off from the supply of fluid circulation from the shear layer. The vorticity level at the vortex centre has dropped to $\zeta' \approx 2$. A vortex typically possesses the highest level of vorticity just before shedding and the vorticity level drops when it is shed and convected downstream (Lam, 1996). Farther downstream in Fig. 14(a), the preceding alternating vortex of clockwise rotation has been convected to $x/D \approx 5$. The vorticity level at its centre has dropped to $\zeta' \approx -1$. This diffusion in peak vorticity level is expected as the vortex increases in size on convecting downstream. The much lower vorticity level is also partly caused by jitter in vortex locations in the ensemble during the phase-lock eduction process.

Fig. 14(b) shows the phase-lock averaged PIV results at the cylinder rotation phase $\theta = \theta_1 + \pi$, that is, half a vortex-shedding cycle later than Fig. 14(a). The two sets of velocity field and vortex pattern are very much up-and-down mirror images of each other. Three vortices are revealed in Fig. 14(b). They are at the same locations as the three vortices in Fig. 14(a) but of the opposite rotation. This confirms a regular vortex street pattern and the two sets of results show the typical flow patterns separated by a half vortex-shedding cycle. Results of similar 180° out-of-phase vorticity contours at half cycles have been obtained in the numerical study of Kang et al. (1999). It should be noted that the ensembles of PIV snapshots at both cylinder rotation phases were obtained in the same experiment without stopping the cylinder rotation. This is because the vortex-shedding phase was not related to a particular cylinder rotation phase in the coincident synchronization between vortex shedding and cylinder rotation.

Vortex properties are analyzed from the ensemble of PIV snapshots at the two vortex-shedding phases. The locations of vorticity peaks are plotted in Fig. 15(a) and they are found to cluster around three densely populated regions. These regions correspond to the most probable locations of three vortices. At the shedding phase $\theta = \theta_1$, these vortices include the growing vortex from the upper shear layer, the mature vortex at the lower shear layer which is about to be shed, and the shed vortex being convected on the upper side of the wake (Fig. 14(a)). Clustering of the vorticity peaks in Fig. 15(a) show that among the three vortices, the centre location of the shed vortex exhibits significant variation among the ensemble. There is also jitter in locations of the two attached vortices but the variations are much smaller. Vortex identification analysis has also been carried out on the PIV snapshots. The results of mean vortex properties are summarized in Table 1 and the ensemble of average vorticity levels are shown in Fig. 15(b). The mean centre positions of the three vortex regions at the shedding phase $\theta = \theta_1$ are at $x/D = 1.2$, 1.7 and 4.4. At the opposite shedding phase, they are at roughly the same streamwise positions $x/D = 1.3$, 1.6 and 4.3. There are, of course, differences in their mean lateral positions due to the sideways deflection of the wake. The corresponding vortex counterparts between the two shedding phases have almost the same vortex sizes (Table 1). There is a bigger difference in size of the two shed vortices where the size determination may be subject to uncertainties due to the choice of the threshold vorticity level in vortex identification. The average vorticity levels between the vortex counterparts are of very similar magnitude but of opposite sign.

The numerical study of Kang et al. (1999) at low Re found that the vorticity contours away from the cylinder surface are similar in overall shape for the alternating vortices shed from either side of the cylinder. However, in the near-surface flow, the vorticity strength on one side of the cylinder becomes more dominant than that on the other side as α increases. It was argued that the rotation effect of the cylinder on the strength of the two shear layers is confined to the flow in the vicinity of the cylinder surface. The present experimental data strengthen this argument. Difference in vortex strengths of the two trains of vortices has been observed in the numerical study of Chew et al. (1995) but only for a limited time during which the cylinder starts to rotate in reaching a steady rotation speed in the numerical experiment. When the flow reaches a steady state of alternate vortex shedding, the shed vortices are found to possess equal strengths. The present results show that there are no noticeable differences in vortex strengths between the two trains of shed vortices in the wake. It seems that the two shear layers feed vorticity to the attaching vortices of opposite signs of rotation which eventually accumulate very similar magnitudes of vorticity or circulation upon shedding.

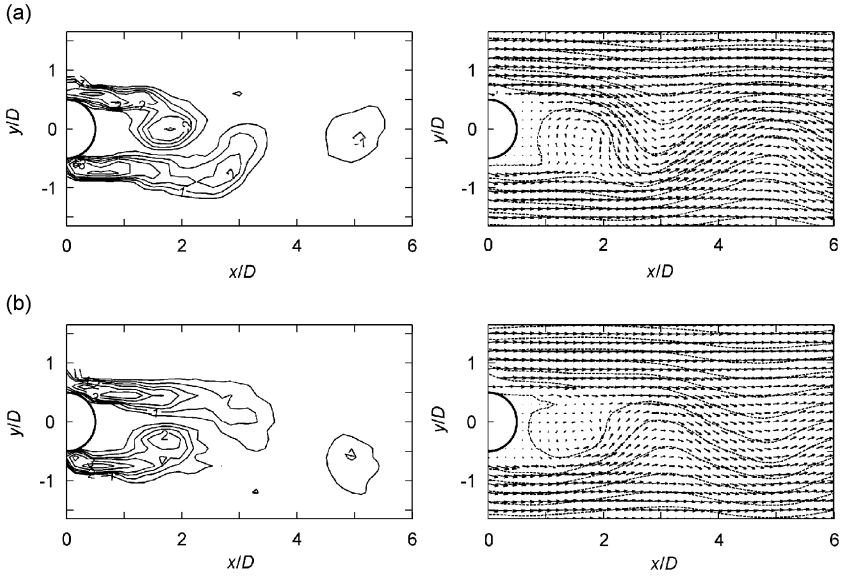

Fig. 14. Phase-lock averaged PIV velocity and vorticity fields and streamlines at $\alpha = 0.65$: vorticity contours shown are in levels $\zeta' = \{\pm 0.5, \pm 1, \pm 1.5, \pm 2, \pm 3, \pm 4, \pm 6, \pm 8\}$.

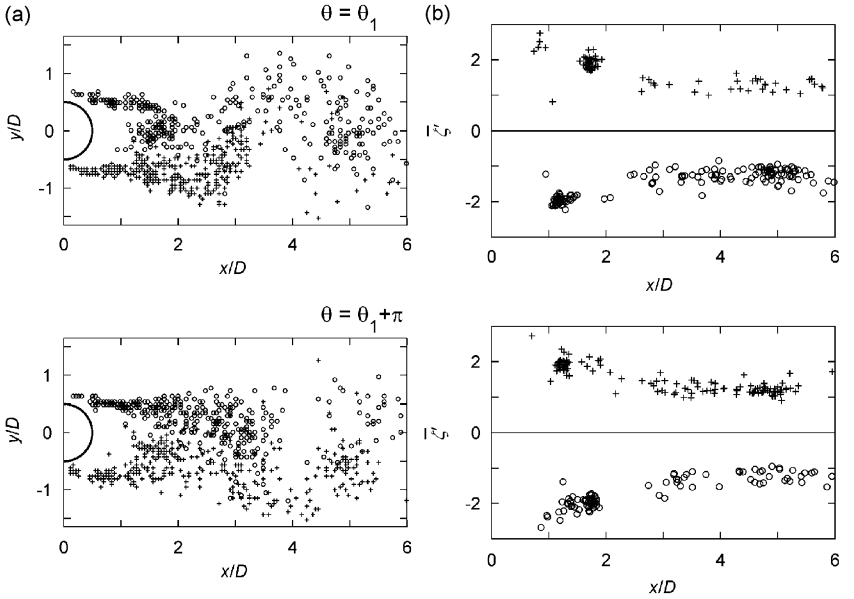

Fig. 15. Vortex properties in ensemble of phase-locked PIV snapshots at $\alpha = 0.65$: (a) locations of vorticity peaks; (b) average vorticity levels of vortex regions. Symbols: (+) positive vorticity; (○) negative vorticity.

Dynamical properties of the three pairs of vortices in Fig. 15 are shown in Fig. 16. Assuming that the shed vortices are convected downstream at a speed $U_c \approx 0.8\, U_\infty$, the flow pattern as it appears to an observer moving with the vortices is thus represented by $(\langle U \rangle - U_c, \langle V \rangle)$, $\langle U \rangle$ and $\langle V \rangle$ being the phase-locked averaged velocity vectors in Fig. 14. This flow pattern shown in Fig. 16 reveals clearly the fluid circulation induced by the shed vortices in the wake. Also shown in Fig. 16 are the coherent Reynolds stresses, $v_c v_c$ and $u_c u_c$, produced by the vortices. The coherent velocity fluctuations, u_c and v_c, are estimated by subtracting the time-averaged mean velocities from the phase-averaged velocities, $u_c = \langle U \rangle - \tilde{U}$ and $v_c = \langle V \rangle - \tilde{V}$. Typical of a vortex street pattern, the alternating vortices jointly produce

Table 1
Mean vortex properties of phase-locked PIV flow fields at $\alpha = 0.65$

	Growing vortex		Mature vortex		Shed vortex	
Shedding phase	$\theta = \theta_1$	$\theta = \theta_1 + \pi$	$\theta = \theta_1$	$\theta = \theta_1 + \pi$	$\theta = \theta_1$	$\theta = \theta_1 + \pi$
Which side of wake	Upper	Lower	Lower	Upper	Upper	Lower
Streamwise centre position, x/D	1.22	1.34	1.72	1.57	4.41	4.27
Lateral centre position, y/D	0.32	−0.57	−0.65	0.37	0.15	−0.73
Total circulation, Γ'	−3.22	3.23	3.83	−3.90	−0.71	0.82
Vortex size, $\lvert\Lambda\rvert/D^2$	1.65	1.68	2.01	1.95	0.58	0.68
Average vorticity level, ζ'	−1.96	1.94	1.91	−2.03	−1.25	1.23

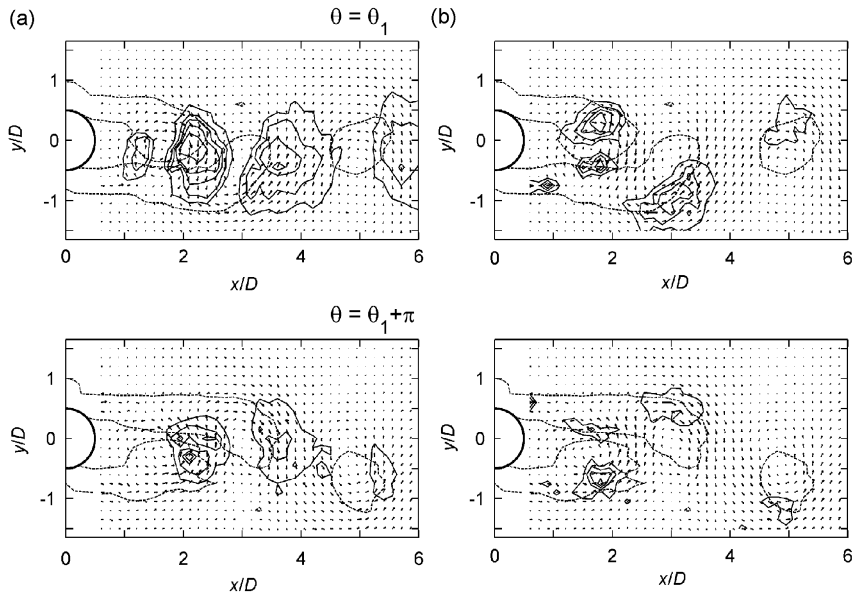

Fig. 16. Velocity vectors as appeared to observer moving forwards at $0.8U_\infty$ and Reynolds stresses associated with vortices in phase-lock averaged PIV flow field at $\alpha = 0.65$: (a) $v_c v_c$; (b) $u_c u_c$. Contours lines are in levels $v_c v_c/U_\infty^2$, or $u_c u_c/U_\infty^2 = \{0.05, 0.1, 0.15, 0.2, 0.3, 0.5\}$. Vorticity contours of $\zeta' = \pm 0.5$ outlined in background.

very high values of $v_c v_c$ in regions between two vortices, while large values of $u_c u_c$ production are found on two lateral sides of each vortex (Cantwell and Coles, 1983).

The phase-locked eduction technique is also applied to the smoke images captured at the particular value of $\alpha = 0.65$. Fig. 17 shows the phase-locked averaged smoke images taken two vortex-shedding phases 180° apart. A clear picture of a vortex street is revealed. This is because almost identical large-scale coherent patterns of the two trains of alternating vortices are repeated in the ensemble of phase-locked smoke images. The alignment of the vortex street and the cylinder wake as a whole is observed to lie at an inclination to the free-stream and deflecting downwards. The vortices in the two phase-locked averaged images are in a symmetrically opposite pattern to each other. This suggests that despite the sideways deflection of the wake, the two trains of vortices on either side of the vortex street remain in a regular alternating pattern.

Although the phase locking of vortex shedding to cylinder rotation at $\alpha = 0.65$ is of a coincident nature rather than due to a physical lock-in mechanism, it may still lead to potentially dangerous resonance phenomena in situations of fluid–structure interaction such as offshore drilling. The torque associated with the cylinder rotation may have periodic fluctuations due to unbalance of mechanical parts and can possibly be amplified by the resonant excitation due to vortex shedding.

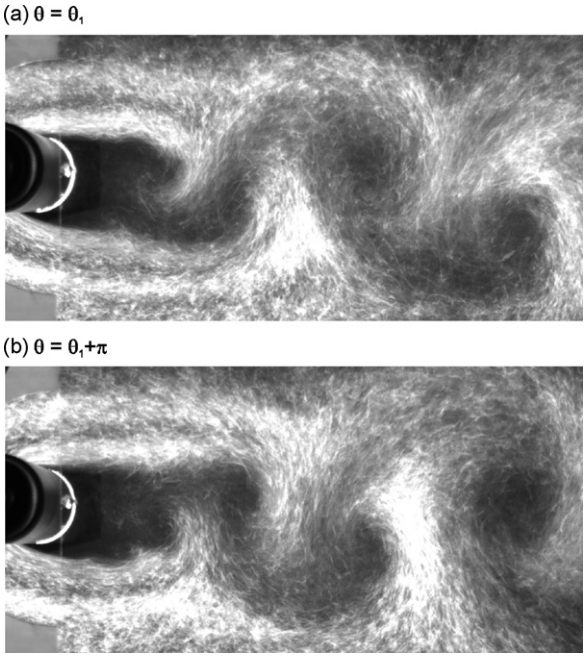

Fig. 17. Phase-lock averaged smoke images at $\alpha = 0.65$.

4. Conclusions

Flow visualizations and PIV measurements are made in the wake behind a steady rotating cylinder at $Re = 3600$–5000 and $\alpha \leqslant 2.5$. Clear evidence of vortex shedding is observed at cylinder rotation speeds lower than $\alpha < 1.9$. The vortex shedding frequency is found to increase with the cylinder rotation speed α. When α increases from 0 to 1, the Strouhal number increases slowly from $St = 0.175$ to 0.23. At the same time, the wake is observed to decrease in width and to be deflected to the side of the wake where the cylinder surface is moving backwards against the free-stream. The vortex formation length is found to decrease with increasing α. Vortex shedding is observed to take place alternatively from the two sides of the rotating cylinder, leading to the pattern of a vortex street in the wake. The global features of the vortex street pattern and dynamics are not much different from those of a stationary cylinder wake, except for a narrower deflected wake and possibly smaller sizes of vortices as α increases. The changes become more significant when α becomes larger than one.

Vorticity fields are derived from the PIV velocity data. Features of the vortex pattern such as the vortex formation length and vortex paths are obtained from a simple analysis of the vorticity peaks. It is observed that vorticity or fluid circulation is fed from either shear layer into an attaching vortex which grows in size and is then shed into the wake. Upon shedding, a very small difference in peak vorticity level is found between the vortices on the two sides of the cylinder. Farther downstream, negligible difference is found on the vortex strength and size between the two trains of shed vortices. A more elaborate analysis is also carried out to identify the large-scale vortices from the vorticity field and to analyze their vortex properties. This provides quantitative information on the effect of cylinder rotation speed on the centre positions, sizes and strength of the vortices. It is found that the vortex formation length is shortened significantly with increasing α, from $\approx 2.5D$ for the stationary cylinder to $\approx 0.65D$ at $\alpha = 1.9$. As α increases, there is noticeable reduction in size of the shed vortices but the average vorticity levels of the shed vortices only drop from $\zeta' \approx 1.4$ at $\alpha = 0$ to $\zeta' \approx 1.0$ at $\alpha = 1.9$.

Synchronization between vortex shedding and cylinder rotation is observed at $\alpha = 0.65$. This lock-in phenomenon is of a coincident nature but provides a convenient opportunity to study the vortex dynamics by the phase-locked averaging technique. Phase-locked averaged smoke visualizations and PIV measurement are carried out at this cylinder rotation speed to investigate the vortex dynamics. The typical structure of a regular and repetitive vortex street is revealed by the velocity vectors and more clearly by the vorticity contours.

Acknowledgements

This investigation was supported by a research grant awarded by the Research Grants Council of Hong Kong (HKU7006/97E). The writer wishes to thank Miss M.W. Wong for her assistance in the experiments.

References

Badr, H.M., Coutanceau, M., Dennis, S.C.R., Menard, C., 1990. Unsteady flow past a rotating circular cylinder at Reynolds numbers 10^3 and 10^4. Journal of Fluid Mechanics 220, 459–484.

Cantwell, B., Coles, D., 1983. An experimental study of entrainment and transport in the turbulent near wake of a circular cylinder. Journal of Fluid Mechanics 136, 321–374.

Chew, Y.T., Cheng, M., Luo, S.C., 1995. A numerical study of flow past a rotating circular cylinder using a hybrid vortex scheme. Journal of Fluid Mechanics 299, 35–71.

Green, R.B., Gerrard, J.H., 1993. Vorticity measurements in the near wake of a circular cylinder at low Reynolds numbers. Journal of Fluid Mechanics 246, 675–691.

Griffin, O.M., Ramberg, S.E., 1976. Vortex shedding from a cylinder vibrating in line with an incident uniform flow. Journal of Fluid Mechanics 75, 257–271.

Ingham, D.B., 1983. Steady flow past a rotating cylinder. Computers and Fluids 11 (4), 351–366.

Kang, S., Choi, H., Lee, S., 1999. Laminar flow past a rotating circular cylinder. Physics of Fluids 11 (11), 3312–3321.

Kimura, T., Tsutahara, M., 1987. Flows about a rotating circular cylinder by the discrete-vortex method. A.I.A.A. Journal 25 (1), 182–184.

Kimura, T., Tsutahara, M., Wang, Z.Y., 1992. Wake of a rotating circular cylinder. A.I.A.A. Journal 30 (2), 555–556.

Lam, K.M., 1996. Phase-locked eduction of vortex shedding in flow past an inclined flat plate. Physics of Fluids 8 (5), 1159–1168.

Lam, K.M., Leung, M.Y.H., 2005. Asymmetric vortex shedding flow past an inclined flat plate at high incidence. European Journal of Mechanics B/Fluids 24, 33–48.

Mittal, S., Kumar, B., 2003. Flow past a rotating cylinder. Journal of Fluid Mechanics 476, 303–334.

Okajima, A., Takata, H., Asanuma, T., 1975. Viscous flow around a rotationally oscillating circular cylinder. Report of the Institute of Space and Aeronautical Science, University of Tokyo, No. 532, pp. 311–338.

Ongoren, A., Rockwell, D., 1988. Flow structure from an oscillating cylinder. Part 1. Mechanisms of phase shift and recovery in the near wake. Journal of Fluid Mechanics 191, 197–223.

Ozono, S., 1999. Flow control of vortex shedding by a short splitter plate asymmetrically arranged downstream of a cylinder. Physics of Fluids 11 (10), 2928–2934.

Sengupta, T.K., Kasliwal, A., De, S., Nair, M., 2003. Temporal flow instability for Magnus–Robins effect at high rotation rates. Journal of Fluids and Structures 17, 941–953.

Stojkovic, D., Schon, P., Breuer, M., Durst, F., 2003. On the new vortex shedding mode past a rotating circular cylinder. Physics of Fluids 15 (5), 1257–1260.

Willert, C.E., Gharib, M., 1991. Digital particle image velocimetry. Experiments in Fluids 10, 181–193.